Intrinsic Coexistence of Miscibility and Segregation in Gold–Silver Nanoalloys

Murilo Moreira, Emmanuel Cottancin, Michel Pellarin, Lucian Roiban, Karine Masenelli-Varlot, Daniel Ugarte, Varlei Rodrigues, Matthias Hillenkamp

Intrinsic coexistence of miscibility and segregation in gold-silver nanoalloys

Murilo Moreira[1,2], Emmanuel Cottancin[1], Michel Pellarin[1], Lucian Roiban[3], Karine Masenelli-Varlot[3], Daniel Ugarte[2], Varlei Rodrigues[2], Matthias Hillenkamp[1,2]*

[1] University Claude Bernard Lyon 1, CNRS, Institute of Light and Matter, UMR5306; Villeurbanne F-69622, France.
[2] Institute of Physics Gleb Wataghin, State University of Campinas; Campinas, SP, 13083-970, Brazil.
[3] University Claude Bernard Lyon 1, INSA Lyon, CNRS, MATEIS, UMR5510; 69621 Villeurbanne, France.
Email: matthias.hillenkamp@univ-lyon1.fr

Keywords: Nanoalloys, nanoparticles, gold, silver, segregation, miscibility, machine learning

Bimetallic nanoparticles are used in numerous applications in catalysis, plasmonics or fuel cell technology. The addition of the second metal to the nanoparticles allows enhancing and fine-tuning their properties by choosing their composition, size, shape and environment. However, the crucial additional parameter of chemical structure within the particle is difficult to predict and access experimentally, even though segregated core-shell structures and random alloys can have drastically different physico-chemical properties. This is highlighted by the vast literature on the most studied bimetallic system, gold-silver, for which the controversy on whether gold and silver are miscible on the nanoscale or segregate persists. Here we solve these contradictions by determining quantitatively the coexistence of an alloyed core and a 1-2 nm-thick shell with gradual silver enrichment as the chemical ground state structure. We furthermore identify chemical reactions with the environment and meta-stable structures as responsible for the contradictions in the literature. Our method is applicable to other multi-metallic systems, provides benchmark input for theoretical models and forms the basis for studying chemical rearrangements under reactive conditions in catalysis.

1. Introduction

Bimetallic nanoparticles (BNPs) have attracted increasing attention in both fundamental and applied sciences in the last decades [1–3] and are expected to play a central role in the ecological transition of our societies. Combining two metals on the nanoscale opens up an entire new playground for the investigation of fundamental physico-chemical properties and offers new degrees of freedom for the tuning of nanoparticle-based devices. Here the nanoparticle properties not only depend on size, shape and environment, but also on their chemical composition and ordering[4]. Different chemical configurations (alloyed vs. segregated, chemically ordered vs. random, etc.) can change considerably the optical, magnetic or catalytic properties. Furthermore, BNPs have been shown not only to permit the replacement of expensive or rare elements with cheaper and more abundant ones, but that unexpected synergies may arise.[5]

One of the most intensely studied bimetallic systems is the gold-silver alloy. Its nanoparticles have attracted large attention for their catalytic,[6,7] plasmonic,[8–10] surface-enhanced sensing [11] and photo-catalytic [12] properties. In the bulk, the two metals are completely miscible across the entire composition range due to the fact that their atomic radius, crystal structure, valence and electronegativity are very similar. On the nanoscale, however, additional degrees of freedom have to be considered, namely surface energy and charge transfer effects, as well as possible segregation and/or chemical ordering into structures inaccessible in the bulk.

Despite the high number of experimental and theoretical articles published on AgAu nanoparticles, the controversy about whether *intrinsically*, i.e., without external influences such as ligands, one of the two metals preferentially segregates at the surface or not is still not resolved, neither on the experimental nor on the theoretical side. Without claim of completeness, we cite hereafter several recent works on this topic to illustrate the contradictions.

Concerning theoretical descriptions, several approaches can be differentiated, some conceptually top-down (macroscopic thermodynamic description with nanoscale corrections), others bottom-up, starting from an atomistic description. A detailed nano-thermodynamic description, used to derive phase diagrams for different crystallographic structures, predicts silver segregation at the nanoparticle surface.[13] A similar surface segregation of Ag was found using crystallographic Wulff constructions.[14]

Many scientists have described the intermediate size range between roughly 2 and 10 nm diameter with atomistic Monte-Carlo or Molecular Dynamics approaches, some of them

combining the two. Whereas complete alloying is found in some cases,[15,16] other authors report a more or less pronounced surface segregation of Ag [17,18] or of Au.[19] As a special case should be considered here simulations predicting alternating layers such as onions [20] or a gold subsurface layer beneath a silver surface.[21] The situation is even more complex for smallest clusters, with ≤ 200 atoms, described by Density Functional Theory (DFT). Here crystalline structure, shell closings and charge transfer are claimed to play an important role. Some articles report preferential surface segregation of Ag,[22] of Au [23,24] or random alloying.[25]

As far as experimental studies are concerned, the overall situation is no less contradictory. In general, two complementary techniques for BNP fabrication have to be distinguished, namely physical and chemical methods. Most of the reported work considers wet-chemically prepared and functionalized AgAu BNPs.[26] Here a wide variety of structures, alloyed vs. Ag@Au vs. Au@Ag, can be synthesized and even interconverted.[27–32] These extensive works show that the choice of synthesis sequence and especially of the surfactant play a dominant role in inducing possible segregation.[32–34]

Physical fabrication techniques comprise sequential pickup in helium droplets,[35,36] laser ablation and condensation in a rare gas [8,37] or liquid [38,39] as well as magnetron sputtering/gas aggregation.[19,40–42] Here the two main reasons for apparent contradictory structural observation are metastability and reactivity. Depending on the fabrication mechanism, the BNPs may be kinetically trapped in metastable ordered or disordered structures. Examples are sequentially grown Ag@Au and Au@Ag core-shell BNPs in He droplets [36] or in gas aggregation sources with varying metal vapor composition.[43] So even though several studies hint at complete alloying for surfactant-free AgAu BNPs,[37,38,40] the efficient mixing might be due to the rapid quenching of the metal vapor. The second process to be considered for physically prepared and thus surfactant-free BNPs is reactivity. Bare metallic AgAu BNPs rapidly react with oxygen upon exposure to air, leading to enrichment of Ag at the surface and eventually to complete separation of silver-oxide from the remaining bare Au cores.[40,42]

All these experiments have in common that the chemical structure of BNPs in the size range <10 nm in diameter, i.e., the range of size effects and highest catalytic activity, is studied only on a qualitative level. This is enough to grossly distinguish between core/shell and fully alloyed structures, but it is insufficient for the detailed analysis required for benchmarking theoretical predictions. Interestingly, we find the same controversy and contradicting results in both experiment and theory also for bulk AgAu alloy surfaces with the additional (inconclusive) discussion of subsurface segregation.[44]

So, all in all, the question whether AgAu on the nanometer scale, relaxed to the ground state and free from surfactants or reactive gases, *intrinsically* forms alloys or segregates to a more or less pronounced degree, is still unresolved. While we can identify external factors (ligands, reactive gases) as responsible for the variety of observed structures, this implies that at least a large fraction of the theoretical simulations of the same systems (pure metallic BNPs in vacuum) is based on erroneous assumptions such as functionals or synergetic effects in properties like surface energies. This is, however, of central importance for the design and optimization of bi- and multi-metallic nanostructures in applications.

The simplest and thus most often used approach for atomistic simulations of bi-(or multi-)metallic structures using DFT is to calculate spherical and surfactant-free nanoparticles in vacuum, often limited to high-symmetry structures such as closed-shell truncated octahedra or icosahedra as ground state structures. The aim of our report is to supply experimental benchmarks for the validation of functionals and simulation procedures, for systems as simple and as close to such simulations as possible. Theoretical structures thus validated can then, e.g., be used to generate Machine Learning Interatomic Potentials (MLIPs) in order to predict materials properties and proceed towards environmental effects such as gases or ligands. If, however, due to lacking experimental references, the presently available theoretic models do not correctly reproduce even the simplest bimetallic system, it will certainly be difficult for them to help in the transition from trial-and-error based development to a controlled approach.

Our work focuses on the size range between 4 and 10 nm diameter. This is small enough to show strong confinement effects due to the surface, if present, and to be of high interest for applications such as in catalysis. At the same time the sizes are big enough to be able to neglect quantum size effects due to a discrete electronic structure and to ensure sufficient particle stability and x-ray counting rates for our quantitative analysis. It is based on a three-fold approach. Firstly, we use surfactant-free AgAu BNPs, combined with annealing in order to provoke relaxation into the chemical ground state. We thus avoid metastability or interface effects to dominate the chemical order within our BNPs. In a second step, we take full profit from recent technological developments permitting element-specific spectroscopy in electron microscopes with unprecedented signal-to-noise ratio. These allow the quantification of composition on the single particle level, complementary to ensemble-averaging techniques such as x-ray diffraction. Lastly, the use of two complementary unsupervised machine learning (ML) techniques, namely principal component analysis (PCA) and non-negative matrix factorization (NMF), permits improved data treatment and statistical validation for the

robust extraction of quantitative information. Even though most of the information necessary for our interpretation is already contained in the raw data, ML considerably accelerates data processing.[45,46] It helps denoising data and deriving spectral and spatial correlations, otherwise difficult to assess. Our approach follows the recently described strategies for accelerating the feedback loop of sample design-characterization-interpretation for nanoscience in general [47] and electron microscopy results in particular.[48]

2. Results and discussion

Pure metallic and surfactant-free AgAu BNPs in the size range between 4-10 nm are fabricated in the gas phase and deposited onto carbon TEM grids. We have very recently demonstrated increased silver segregation at the surface of AgAu BNPs exposed to air. In order to exclude such extrinsic oxidation effects in the present study, the particles are capped with a ~20 nm layer of amorphous carbon. This latter procedure has been shown to efficiently protect BNPs against oxidation.[49,50] Both silver and gold are essentially insoluble in carbon [51,52] so we expect the matrix to interact only very weakly with the BNPs and we consider its influence on the chemical order of the AgAu BNPs as negligible. Embedding in amorphous carbon furthermore permits annealing the samples in vacuum without deteriorating the size distribution,[49,50] thereby relaxing the BNPs towards their chemical ground state.

The BNPs are characterized by scanning transmission electron microscopy (STEM). We notably perform imaging in the STEM-HAADF mode (High Angle Annular Dark Field) and energy-dispersive X-ray spectroscopy (STEM-EDX). In the latter, the electron beam is focused to 0.3 nm in diameter and scanned across a defined sample area. At each pixel, a complete x-ray spectrum containing element-specific emission lines for all elements present in the sample is recorded, thereby forming a three-dimensional hyperspectral image. We have recently demonstrated that not only the chemical composition can be quantified on the individual particle level,[41] but that if sufficient counting rates are attained, it is possible to perform spatially resolved quantifications with error bars of the order of 2-3 at.%.[42]

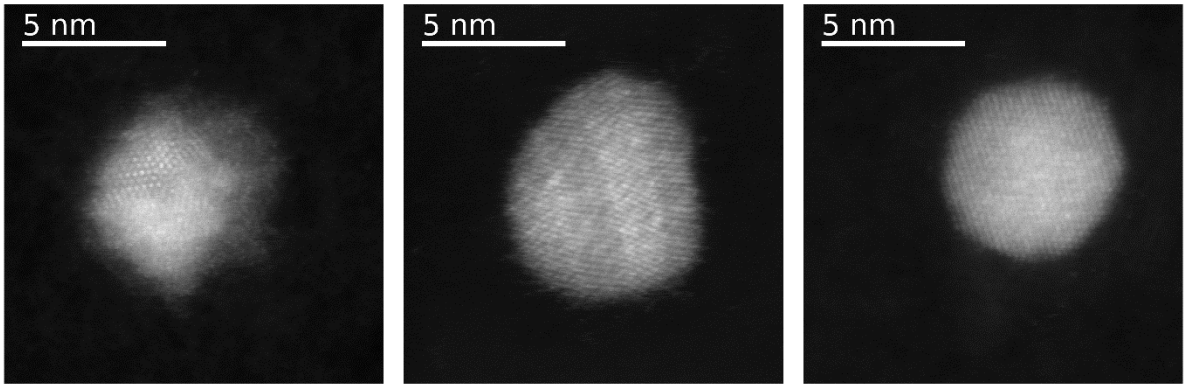

Figure 1: AgAu BNP Images. STEM-HAADF images of unprotected (left), protected (center) and annealed (right) AgAu BNPs. The amorphous oxide shell is clearly visible in Fig. 1a but absent in the other two images.

Fig. 1a shows a HAADF image of a representative unprotected AgAu BNP after exposure to ambient air. An amorphous layer is visible around the particles, which we attribute to silver ageing through reactions with ambient oxygen.[53] As reported qualitatively before,[40] ageing promotes migration of silver atoms to the particle surface. When capping identical BNPs with ~20 nm of amorphous carbon, no more amorphous oxide at the BNP surface is evidenced at the BNP surface: the particles are effectively protected (cf. Fig. 1b). In order to ensure that these AgAu BNPs are not trapped in metastable configurations, we next anneal them in vacuum for 2h at 573 K in order to promote chemical order relaxation. The first obvious consequence of annealing is an increase in crystal domain size inside the BNPs, as evidenced by selected area electron diffraction (cf. Supporting Materials, figure SI1.2), underlining restructuring and defect relaxation (twins and stacking faults). In the following, we focus on the thorough analysis of relaxed BNPs, 118 in total.

In order to infer the chemical structure within BNPs, lateral profiles are typically derived, as shown in Figs. 2a and b. While some deviations from perfect alloying are already qualitatively visible, it is, however, difficult to affirm segregation. We thus use a recently developed protocol [42] which allows us to obtain quantitative radial composition profiles. Here we integrate the EDX signals for Ag and Au azimuthally around the projected center of the BNP and obtain the radial chemical gradients for individual BNPs with a spatial step size of 0.5 nm (see methods). Even though not unambiguously visible in the radial profiles such as in Fig. 2b, the chemical gradients of all BNPs consistently show a gradual enrichment of Ag towards the BNP surface rather than a solid solution or well-segregated core-shell structure. This Ag surface enrichment is robustly confirmed by the non-overlapping 3σ uncertainty

intervals [42] at the nanoparticle center (C_{Ag} = 0.49 ± 0.01) and surface (C_{Ag} = 0.58 ± 0.01). All derived gradients for BNP ensemble studied here are shown in the Supporting Information.

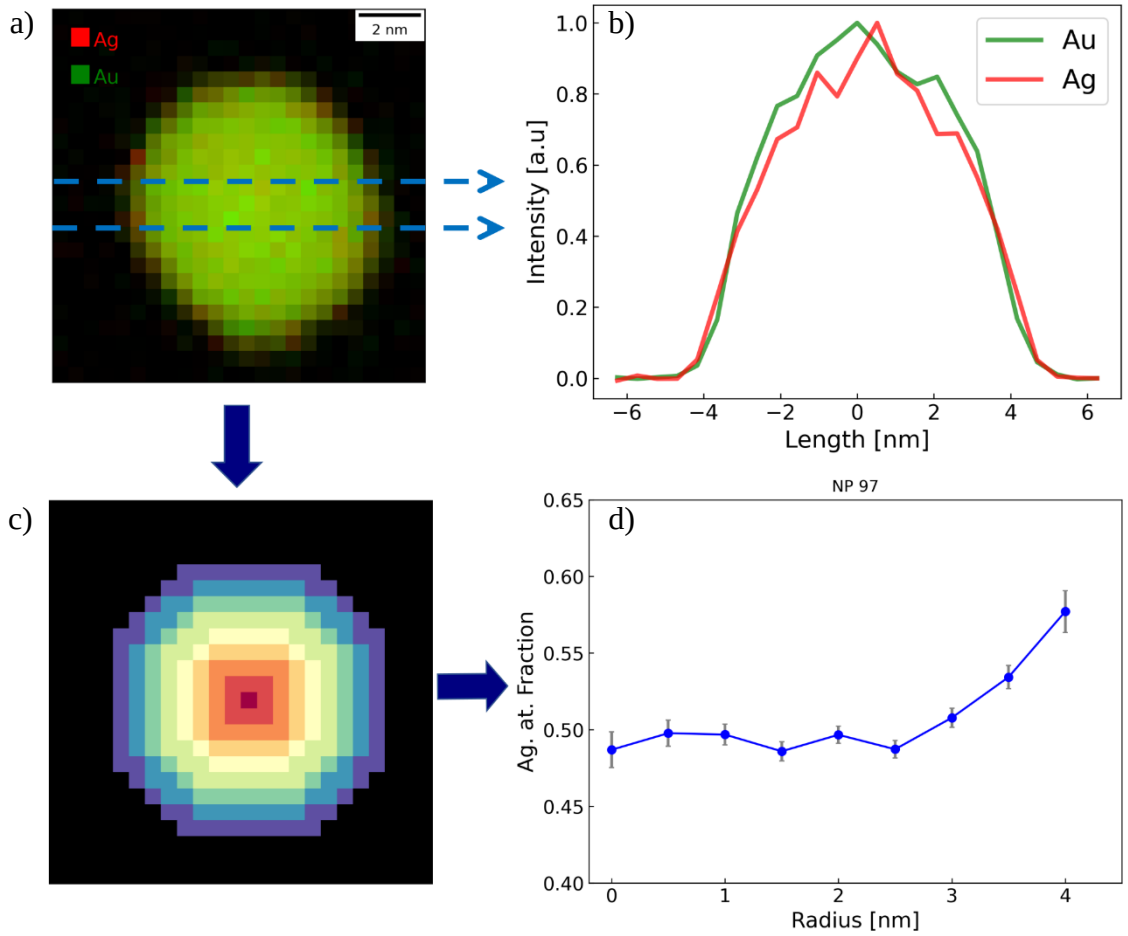

Figure 2: Chemical order. a) EDX map of an annealed AgAu BNP of 8 nm diameter. b) Three-pixel wide normalized elemental profiles for Ag and Au. c) Concentric rings of thickness 0.5 nm are defined in the projected image and shown in colour code. Their azimuthal integration of Ag and Au signals yields radial chemical gradients, as shown in d). The error bars reflect the propagation of Poisson noise and background subtraction.

These results allow a detailed discussion of the intrinsic nanoscale miscibility of gold and silver. In order to better evidence trends and size effects, we regroup the individual chemical gradients as a function of diameter, as shown in Fig. 3a. This figure allows evidencing subtle differences in chemical structure that are not resolved in conventional qualitative chemical mapping as in figures 2a and b. Considering that the BNPs have attained their chemical ground state after protection and annealing, the plots reveal two distinct regions in the BNPs:

an almost constant Ag fraction in the core of the particle and a shell with increasing Ag percentage and a thickness of ~1-2 nm.

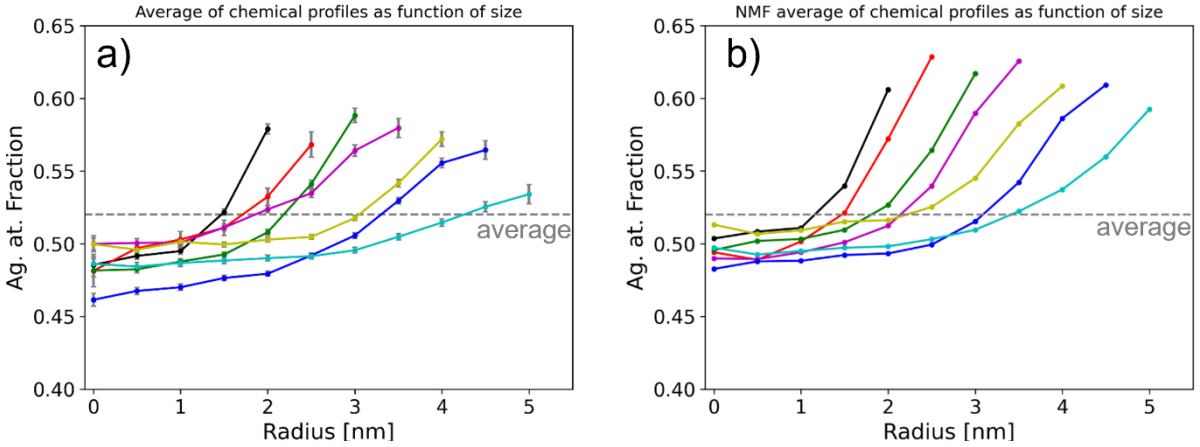

Figure 3: Chemical gradients for different AgAu BNP diameters. Left: averaged raw data (quantitative chemical analysis); right: NMF denoised and averaged data. The higher signal-to-noise ratio after NMF processing permits including more data at the particle surface (see text). No error bars are displayed for the NMF denoised data as their calculation does not yet follow a recognized and well accepted procedure. The dashed lines represent the mean Ag fraction as averaged over the entire BNP ensemble.

In order to improve the quality and statistical reliability of our study, we perform unsupervised machine learning with several aims. Firstly, it is applied for denoising, the standard procedure for removing a large fraction of Poisson noise.[54,55] We first used PCA in order to determine the necessary number of components to correctly reproduce all relevant spectral information to eight. We then use NMF for a physically meaningful decomposition of the EDX signals. Here only two of the eight NMF components contain Au and Ag EDX signals from the BNPs. Whereas component NMF#1 accounts for all the gold and a minimum of silver in each pixel spectrum, component NMF#7 reflects the additional amount of silver required to reproduce spatial variations in chemical composition (cf. Fig. 4). All other detected elements and corresponding NMF components originate from the microscopy grid, the sample holder and the x-ray detector. This demonstrates that our linear unmixing results in successful blind source separation of background and BNP-related signal and permits further validation of our interpretation. The clear separation of BNP-related and uncorrelated signal underlines the high sample quality and the attained EDX signal-to-noise ratio. We insist that we do not find any correlations between the Au and Ag signals in the BNPs and any

contaminants (other elements in the EDX spectra) that might influence the chemical order within them, such as Oxygen, Chlorine or Sulfur.

In Fig. 3b are displayed the averaged chemical gradients after NMF denoising. Here the distinction between homogeneous alloyed core and the shell with continuous increase in Ag is better visible than in the raw data. Today no standard procedure for error propagation after NMF denoising of hyperspectral data exists but we have recently shown that for entire BNPs PCA reduces the errors by a factor 2-3, i.e. into the range of the percent in atomic fraction.[54,55] We can thus safely assume that the effective errors for Fig. 3b are at least as small as in Fig. 3a, for which error propagation was calculated following standard procedures.[55]

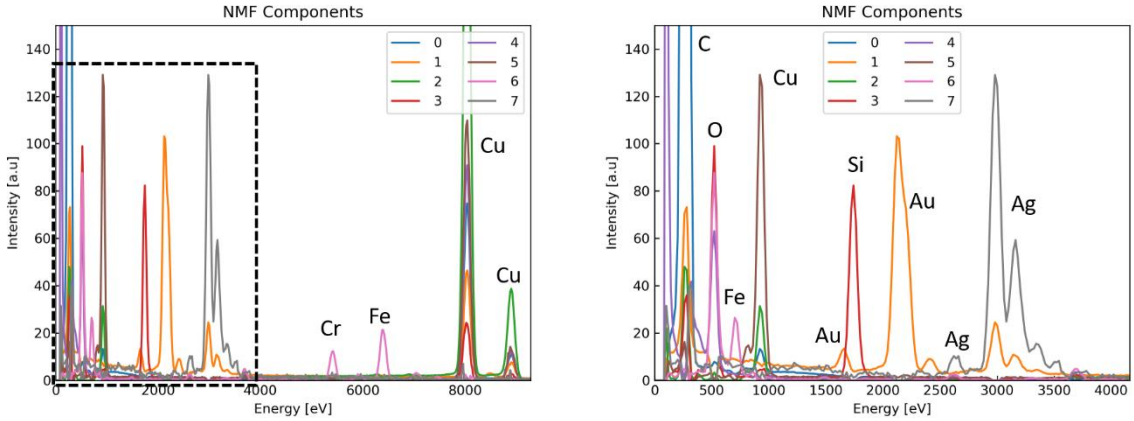

Figure 4: Decomposition of x-ray signals. Overview of the eight components derived by NMF to describe the element-specific x-ray lines of our sample. Only components NMF#1 and NMF#7 account for Au and Ag in the BNPs, all other components correspond to signal from the substrate or the microscope. The right panel shows a zoom of the low-energy region delimited by the dashed box.

Reconstructing the particle EDX spectra with only the two BNP-related NMF components permits a better definition of the particle size and furthermore allows us to separate BNP-related and background signals. This results in a better fitting of the EDX peaks for a chemical composition analysis and thus improves the detection limit, as described in more detail in the Supporting Information. Consequently, our averaged NMF gradients in Fig. 3b include more information close to the BNP surface and we observe an enhanced segregation as compared to the raw data (Fig. 3a).

We have derived our quantitative chemical gradients for two-dimensional projections of the BNPs. We note, however, that this does not affect the validity of our interpretations. The

relaxed BNPs are isotropically surrounded by carbon and we see no reason for the projection not to be representative of the three-dimensional chemical structure.

From these observations, we derive that Au and Ag are indeed miscible within the volume, even if this core is only ~2 nm across, i.e., containing around ~250 atoms. At the BNP surface, surrounding this core, we consistently find partial segregation of silver, which is, however, more complex than what was previously reported. We neither observe distinct core-shell structures with neat interfaces, nor enrichment only in the outermost layer of the BNP. Although we cannot resolve individual layers,[56] we can quantify a continuous increase in Ag fraction with analytical precision, even if it is as small as ~10%. We identify the chemical reactions with the environment (surfactants, oxidizing atmosphere, etc.) and metastable structures as obtained in different fabrication processes as responsible for the contradictions in the literature.

These results demonstrate that simplified approaches considering only the surface layer or representing the BNP as a two-phase core-shell structure with elemental separation are insufficient to correctly describe their chemical structure. This also means that the BNP chemical structure cannot be directly inferred from bulk surface results. Even setting aside the contradictions in the literature as to whether Au or Ag segregates at the bulk surface,[44] none of the existing articles, to our knowledge, considers deviations from bulk miscibility below the sub-surface layer, i.e. only across ≤5 Å.

Conclusion

We conclude that gold and silver are miscible even on the nanoscale but that in the chemical ground state a slight and gradual Ag enrichment of the order of ~10% is measurable in a surface layer of ~1-2 nm thickness. No size effects have been evidenced in the investigated range of 4-10 nm diameter. These results settle the ongoing controversy about alloying or segregation and of which metal is enriched at the AgAu BNP surface, at least down to sizes of 4 nm in diameter. These findings provide crucial benchmark input for the validation of theoretical approaches, notably of the validity of nanothermodynamic descriptions and for the critical evaluation of charge transfer processes as incorporated in density functional theory models.[23,25,44] A correct description of pure metallic BNPs can then serve as starting point for the prediction of non-spherical particles and the influence of an environment (ligands, reactive gases etc.).

The implications of our work go well beyond the question of nanoscale miscibility of gold and silver. Accelerating the feedback loop of design, characterization and optimization of

BNPs in materials central for the ecological transition relies, amongst others, on the supply of chemical ground state structures as benchmark input for the development and validation of interatomic potentials.[47,48] Our approach, combining experimental characterization and machine learning based data processing, is applicable to a very large number of elemental combinations up to high-entropy alloys and to geometries other than nanoparticles. Especially the combination with environmental investigations [57] promises access to chemically induced restructuring in BNPs upon exposure to reactive gases,[58] information essential for understanding and improving catalytic activity, selectivity and stability.[59]

Methods

Sample fabrication and characterization

Surfactant-free AgAu BNPs are fabricated in the gas phase using a laser vaporization cluster source. Here a doubled Nd:YAG laser (532 nm) is focused onto the surface of an $Ag_{50}Au_{50}$ target rod and the generated plasma is quenched in a continuous He/Ar flow. Nanoparticles form in the volume of approximately one cm above the target before being swept into vacuum through a 0.6 mm nozzle, creating a supersonic expansion. The charged fraction of the nanoparticle beam is then mass-selected in a quadrupole deviator [60] before being deposited fragmentation-free onto TEM grids under UHV conditions ($<10^{-9}$ mbar).

The AgAu BNPs are then covered in-situ by a layer of amorphous carbon of ~20 nm thickness, thick enough to efficiently protect the particles against oxidation but thin enough to allow (S)TEM-based imaging and spectroscopy. Here carbon filaments of ~2 mm thickness are flashed by passing a sudden current of >10 A, thereby depositing an average of ~5 nm of amorphous carbon onto the sample at a defined distance. Several previous experiments with BNPs fabricated in the same laser vaporization cluster source have shown that the as prepared BNPs are often chemically disordered due to the rapid condensation and quenching during fabrication, especially for alloys with comparably high melting temperatures. CoPt BNPs, for example, display random chemical structures with very low magnetic anisotropy that can be thermally relaxed into high-anisotropy, ordered $L1_0$ structures.[49] In order to promote atomic diffusion within our AgAu BNPs towards the lowest energy chemical distribution, we annealed the carbon-protected nanoparticles for 2 h at 573 K in vacuum (~$1*10^{-7}$ mbar). This temperature is close to the size-dependent melting point of AgAu BNPs (~800 K for 5 nm diameter [36]). A recent study has furthermore demonstrated an increase of the diffusion constant in AgAu BNPs of several orders of magnitude as a function of defect density.[61]

Some particles described in this reference undergo significant chemical order changes even at room temperature. We can thus expect our BNPs, which initially show considerable amounts of defects, twinning and polycrystallinity, to be in the thermodynamic ground state in these annealed samples, at least as far as the chemical structure is concerned. This enhanced atomic mobility is supported by the increase in crystallite size, as evidenced by electron diffraction (cf. Fig. SI1.2).

We observed no signs of degradation of the carbon films, which could be catalyzed by the presence of the BNPs, neither after heat treatment nor during STEM investigation. The average chemical composition was measured to $Ag_{52}Au_{48}$ on the entire ensemble of BNPs. No beam-induced change in size or chemical composition was detected throughout the investigation of individual BNPs.

STEM-EDX experiments have been performed with a JEOL Neo-ARM Cold-FEG at the Hubert Curien Laboratory, equipped with a Silicon Drift Detector (SDD) JEOL CENTURIO with approximately 1 sr of solid angle for x-ray collection. The acceleration voltage was set to 80 keV in order to increase ionization efficiency and exclude knock-on damage. The acquisition parameters were: beam diameter 0.3 nm, 0.25 nm for the pixel step, and a dwell time of ~100 ms per pixel; the image size was set to 4096 energy channels and 64x64 pixels with typically 1-2 NPs per image. Two-dimensional images with an X-ray spectrum in the third dimension for each pixel form the so-called datacubes or hyperspectral images. In order to minimize dose rate, a series of images of the same region was acquired and subsequently individual frames were added (100 scans at 1 ms dwell time).[62] For all experiments a low background Be sample holder was used. Raw EDX spectra were binned to 1024 energy channels to increase signal-to-noise ratio, leading to an EDX channel width of 20 eV. Similarly, the pixels were binned to 0.5 nm pixel size to increase signal-to-noise ratio. The integrated signal from the Au-Mα and Ag-Lα EDX peaks has been used to perform chemical composition calculations. The background signal was separately fitted for the raw and PCA denoised data, whereas it is strongly reduced in the reconstructed data using only NMF components NMF#1 and 7. As quantification limit, we consistently use the criterion $I > 10\sigma_0$ [63], where $\sigma_0 = \sqrt{\sigma_I^2 + \sigma_{Ib}^2}$ ($\sigma_I^2 = I$ and $\sigma_{Ib}^2 = I$ are the Poisson uncertainties of the integrated Ag and Au peaks and their background subtracted contribution, respectively).

The quantitative analysis of the individual BNP chemical composition followed the Cliff-Lorimer approach [64] using an experimentally measured K_{AB} = 1.44 ± 0.01 factor which has been measured using a thin film of known composition:

$$\frac{C_A}{C_B} = K_{AB}\frac{I_{A,NP}}{I_{B,NP}}$$

with C_y and I_y, NP the atomic percentage and X-ray intensity of element y per NP, respectively.

Estimations of chemical composition and their error bars have taken into account all quantitative EDX analysis steps applied on a fitted curve of the experimental EDX spectra (background removal, X-ray peak integration and composition determination); we have considered Poisson noise for all EDX count measurements. We underline the analytical quality of our EDX data as the derived degrees in segregation are larger than the 3σ uncertainty interval [55] for all averaged profiles of Fig. 3 and most of the individual gradients displayed in section SI4. An example spectrum of an entire BNP is shown in Fig. SI3.1.

All EDX and ML processing steps have been performed using the open-source Hyperspy Python library.[65]

PCA and NMF data processing

All data were first treated using principal component analysis in order to evaluate the number of necessary components and then by non-negative matrix factorization. Both methods allow denoising plus a statistical analysis in the sense that they permit retrieving latent correlations.

In PCA, the raw data are decomposed into a number of orthogonal eigenvectors, termed loadings. The correlation between the spectra associated with a certain pixel and a particular eigenvector gives an amplitude for that specific component, the score. By diagonalizing the covariance matrix that represents the data set, it is possible to derive from a scree plot (cf. figure SI3.3) the number of principal components (eigenvectors) to describe the physical system and to separate them from omnipresent Poisson noise.[54,55] Reconstructing the data with only the first eight eigenvectors permits removing a large fraction of uncorrelated noise without losing the physical signal, which is thus denoised. The scatter of compositional values around a mean value is reduced and we have calculated the remaining error for entire AgAu BNPs to be reduced by a factor 2-3.[55] We recall here that the spectra in denoised reconstructed datacubes do not represent independent measurements but are fully correlated.

The individual PCA components are, however, not easily interpretable. PCA does not perform an efficient blind source separation and all physical signals are present in all components, with positive or negative scores (cf. Fig. SI3.4).

NMF is a complementary ML technique for linear decomposition, which is particularly suited for evidencing spectral and spatial correlations and, as it allows only positive signals, a physical interpretation of the components is often easier. The application of NMF processing requires that the number of components be defined in advance and we use eight components as deduced from PCA. These components reproduce all physically real signals: two (NMF#1 and #7) are needed for the AgAu BNPs and six others for the different background and spurious signals and their relative variations. In our AgAu systems, the interpretation of the different components is thus comparably straightforward.

A comprehensive overview of our ML treated data is given in the SI.

Supporting Information

Supporting Information is available from the Wiley Online Library or from the author.

Acknowledgements

All samples were elaborated at the PLYRA@iLMtech facility with technical support from O. Boisron, C. Albin, C. Clavier and S. Hermelin. The authors also thank N. Blanchard, S. Reynaud and Y. Lefkir for technical support at the Consortium Lyon Saint-Etienne de Microscopie (CLYM). CLYM and Laboratoire Hubert Curien are acknowledged for the access to the microscope. Financial support is acknowledged from the French National Research Agency (ANR) via the projects ‘SchNAPSS’ (ANR-21-CE09-0021) and ‘NACRE’ (ANR-23-PEXD-0015), the latter in the France 2030 framework of PEPR DIADEM. Further support by the French Campus France Eiffel Excellency Scholarship Program (EIFFEL-DOCTORAT 2020/P760767) for M.M. is acknowledged. Funding from CNPq (No. 162541/2018-0, 402676/2021-1, 303025/2022-0), FAPESP (2020/15497-1) and access to the FEG-TEM/STEM from the Brazilian Nanotechnology National Laboratory (LNNANO, grant No. ME – 22329) are acknowledged. This work was supported by the international research network IRN Nanoalloys of the CNRS.

Received: ((will be filled in by the editorial staff))
Revised: ((will be filled in by the editorial staff))
Published online: ((will be filled in by the editorial staff))

References

(1) *Nanoalloys: Synthesis, Structure and Properties*; Alloyeau, D., Mottet, C., Ricolleau, C., Eds.; Engineering Materials; Springer: London, 2012. https://doi.org/10.1007/978-1-4471-4014-6.

(2) Ferrando, R. *Structure and Properties of Nanoalloys*; Elsevier, 2017; Vol. 10.

(3) *Nanoalloys: From Fundamentals to Emergent Applications*; Calvo, F., Ed.; Elsevier: Oxford, 2020. https://doi.org/10.1016/B978-0-12-819847-6.00002-4.

(4) Tao, F.; Salmeron, M. Surface Restructuring and Predictive Design of Heterogeneous Catalysts. *Science* **2024**, *386* (6724), eadq0102. https://doi.org/10.1126/science.adq0102.

(5) Piccolo, L. Surface Studies of Catalysis by Metals: Nanosize and Alloying Effects. In *Nanoalloys: Synthesis, Structure and Properties*; Alloyeau, D., Mottet, C., Ricolleau, C., Eds.; Springer: London, 2012; pp 369–404. https://doi.org/10.1007/978-1-4471-4014-6_11.

(6) Liu, J.-H.; Wang, A.-Q.; Chi, Y.-S.; Lin, H.-P.; Mou, C.-Y. Synergistic Effect in an Au-Ag Alloy Nanocatalyst: CO Oxidation. *J Phys Chem B* **2005**, *109*, 40–43. https://doi.org/10.1021/jp044938g.

(7) Tokonami, S.; Morita, N.; Takasaki, K.; Toshima, N. Novel Synthesis, Structure, and Oxidation Catalysis of Ag/Au Bimetallic Nanoparticles. *J Phys Chem C* **2010**, *114*, 10336–10341. https://doi.org/10.1021/jp9119149.

(8) Gaudry, M.; Lermé, J.; Cottancin, E.; Pellarin, M.; Vialle, J.-L.; Broyer, M.; Prével, B.; Treilleux, M.; Mélinon, P. Optical Properties of (AuxAg1-x)n Clusters Embedded in Alumina: Evolution with Size and Stoichiometry. *Phys. Rev. B* **2001**, *64* (8), 085407. https://doi.org/10.1103/PhysRevB.64.085407.

(9) Cha, S. K.; Mun, J. H.; Chang, T.; Kim, S. Y.; Kim, J. Y.; Jin, H. M.; Lee, J. Y.; Shin, J.; Kim, K. H.; Kim, S. O. Au–Ag Core–Shell Nanoparticle Array by Block Copolymer Lithography for Synergistic Broadband Plasmonic Properties. *ACS Nano* **2015**, *9*, 5536–5543. https://doi.org/10.1021/acsnano.5b01641.

(10) Weissker, H.-C.; Calvo, F. Optical Properties of AgAu Alloy Clusters: Effect of Chemical Configuration along a Rearrangement Pathway. *Alloys* **2024**, *3* (1), 31–42. https://doi.org/10.3390/alloys3010003.

(11) Girao, A. V.; Pinheiro, P. C.; Ferro, M.; Trindade, T. Tailoring Gold and Silver Colloidal Bimetallic Nanoalloys towards SERS Detection of Rhodamine 6G. *RSC Adv* **2017**, *7*, 15944-15951-15944–15951. https://doi.org/10.1039/C7RA00685C.

(12) Wang, J. L.; Ando, R. A.; Camargo, P. H. C. Investigating the Plasmon-Mediated Catalytic Activity of AgAu Nanoparticles as a Function of Composition: Are Two Metals Better than One? *ACS Catal* **2014**, *4*, 3815–3819. https://doi.org/10.1021/cs501189m.

(13) Guisbiers, G.; Mendoza-Cruz, R.; Bazán-Díaz, L.; Velázquez-Salazar, J. J.; Mendoza-Perez, R.; Robledo-Torres, J. A.; Rodriguez-Lopez, J.-L.; Montejano-Carrizales, J. M.; Whetten, R. L.; José-Yacamán, M. Electrum, the Gold–Silver Alloy, from the Bulk Scale to the Nanoscale: Synthesis, Properties, and Segregation Rules. *ACS Nano* **2016**, *10* (1), 188–198. https://doi.org/10.1021/acsnano.5b05755.

(14) Ringe, E.; Duyne, R. P. V.; Marks, L. D. Wulff Construction for Alloy Nanoparticles. *Nano Lett* **2011**, *11*, 3399–3403. https://doi.org/10.1021/nl2018146.

(15) Calvo, F.; Cottancin, E.; Broyer, M. Segregation, Core Alloying, and Shape Transitions in Bimetallic Nanoclusters: Monte Carlo Simulations. *Phys Rev B* **2008**, *77*, 121406–121406. https://doi.org/10.1103/PhysRevB.77.121406.

(16) Qi, W. H.; Lee, S. T. Phase Stability, Melting, and Alloy Formation of Au−Ag Bimetallic Nanoparticles. *J Phys Chem C* **2010**, *114*, 9580–9587. https://doi.org/10.1021/jp9113442.

(17) Eom, N.; Messing, M. E.; Johansson, J.; Deppert, K. General Trends in Core–Shell Preferences for Bimetallic Nanoparticles. *ACS Nano* **2021**, *15*, 8883–8895. https://doi.org/10.1021/acsnano.1c01500.
(18) Koraychy, E. yakout E.; Nelli, D.; Roncaglia, C.; Minnai, C.; Ferrando, R. Growth of Size-Matched Nanoalloys – a Comparison of AuAg and PtPd. *Eur. Phys. J. Appl. Phys.* **2022**, *97*, 28. https://doi.org/10.1051/epjap/2022210297.
(19) Gromoff, Q.; Benzo, P.; Saidi, W. A.; Andolina, C. M.; Casanove, M.-J.; Hungria, T.; Barre, S.; Benoit, M.; Lam, J. Exploring the Formation of Gold/Silver Nanoalloys with Gas-Phase Synthesis and Machine-Learning Assisted Simulations. *Nanoscale* **2023**, *16* (1), 384–393. https://doi.org/10.1039/D3NR04471H.
(20) Cheng, D.; Wang, W.; Huang, S.; Cao, D. Atomistic Modeling of Multishell Onion-Ring Bimetallic Nanowires and Clusters. *J Phys Chem C* **2008**, *112*, 4855–4860. https://doi.org/10.1021/jp0776863.
(21) Deng, L.; Hu, W.; Deng, H.; Xiao, S.; Tang, J. Au–Ag Bimetallic Nanoparticles: Surface Segregation and Atomic-Scale Structure. *J Phys Chem C* **2011**, *115* (23), 11355–11363. https://doi.org/10.1021/jp200642d.
(22) Chen, F.; Johnston, R. L. Energetic, Electronic, and Thermal Effects on Structural Properties of Ag-Au Nanoalloys. *ACS Nano* **2008**, *2*, 165–175. https://doi.org/10.1021/nn700226y.
(23) Rapetti, D.; Ferrando, R. Density Functional Theory Global Optimization of Chemical Ordering in AgAu Nanoalloys. *J Alloy Comp* **2019**, *779*, 582–589. https://doi.org/10.1016/j.jallcom.2018.11.143.
(24) Ghosh, A.; Datta, S.; Saha-Dasgupta, T. Understanding the Trend in Core–Shell Preferences for Bimetallic Nanoclusters: A Machine Learning Approach. *J Phys Chem C* **2022**, *126*, 6847–6853. https://doi.org/10.1021/acs.jpcc.2c01096.
(25) Cerbelaud, M.; Ferrando, R.; Barcaro, G.; Fortunelli, A. Optimization of Chemical Ordering in AgAu Nanoalloys. *Phys Chem Chem Phys* **2011**, *13*, 10232–10232. https://doi.org/10.1039/c0cp02845b.
(26) Cortie, M. B.; McDonagh, A. M. Synthesis and Optical Properties of Hybrid and Alloy Plasmonic Nanoparticles. *Chem Rev* **2011**, *111*, 3713–3735. https://doi.org/10.1021/cr1002529.
(27) Wilcoxon, J. P.; Provencio, P. P. Heterogeneous Growth of Metal Clusters from Solutions of Seed Nanoparticles. *J Am Chem Soc* **2004**, *126*, 6402–6408. https://doi.org/10.1021/ja031622y.
(28) Chen, H. M.; Liu, R. S.; Jang, L.-Y.; Lee, J.-F.; Hu, S. F. Characterization of Core–Shell Type and Alloy Ag/Au Bimetallic Clusters by Using Extended X-Ray Absorption Fine Structure Spectroscopy. *Chem Phys Lett* **2006**, *421*, 118–123. https://doi.org/10.1016/j.cplett.2006.01.043.
(29) Li, Z. Y.; Wilcoxon, J. P.; Yin, F.; Chen, Y.; Palmer, R. E.; Johnston, R. L. Structures and Optical Properties of 4–5 Nm Bimetallic AgAu Nanoparticles. *Faraday Discuss* **2008**, *138*, 363–373. https://doi.org/10.1039/b708958a.
(30) Gilroy, K. D.; Ruditskiy, A.; Peng, H.-C.; Qin, D.; Xia, Y. Bimetallic Nanocrystals: Syntheses, Properties, and Applications. *Chem Rev* **2016**, *116*, 10414–10472. https://doi.org/10.1021/acs.chemrev.6b00211.
(31) Mendoza-Cruz, R.; Palomares-Báez, J. P.; López-López, S. M.; Montejano-Carrizales, J. M.; Rodríguez López, J. L.; José Yacamán, M.; Bazán-Díaz, L. Experimental High-Resolution Observation of the Truncated Double-Icosahedron Structure: A Stable Twinned Shell in Alloyed Au–Ag Core@Shell Nanoparticles. *Nano Lett.* **2024**, *24* (14), 4072–4081. https://doi.org/10.1021/acs.nanolett.3c04435.

(32) Gonzalez, C. M.; Liu, Y.; Scaiano, J. C. Photochemical Strategies for the Facile Synthesis of Gold-Silver Alloy and Core-Shell Bimetallic Nanoparticles. *J Phys Chem C* **2009**, *113*, 11861–11867. https://doi.org/10.1021/jp902061v.
(33) Feng, Y.; He, J.; Wang, H.; Tay, Y. Y.; Sun, H.; Zhu, L.; Chen, H. An Unconventional Role of Ligand in Continuously Tuning of Metal–Metal Interfacial Strain. *J Am Chem Soc* **2012**, *134*, 2004–2007. https://doi.org/10.1021/ja211086y.
(34) Skorikov, A.; Albrecht, W.; Bladt, E.; Xie, X.; van der Hoeven, J. E. S.; van Blaaderen, A.; Van Aert, S.; Bals, S. Quantitative 3D Characterization of Elemental Diffusion Dynamics in Individual Ag@Au Nanoparticles with Different Shapes. *ACS Nano* **2019**, *13* (11), 13421–13429. https://doi.org/10.1021/acsnano.9b06848.
(35) Haberfehlner, G.; Thaler, P.; Knez, D.; Volk, A.; Hofer, F.; Ernst, W. E.; Kothleitner, G. Formation of Bimetallic Clusters in Superfluid Helium Nanodroplets Analysed by Atomic Resolution Electron Tomography. *Nat Commun* **2015**, *6*, 8779–8779. https://doi.org/10.1002/9783527808465.emc2016.4672.
(36) Lasserus, M.; Schnedlitz, M.; Knez, D.; Messner, R.; Schiffmann, A.; Lackner, F.; Hauser, A. W.; Hofer, F.; Ernst, W. E. Thermally Induced Alloying Processes in a Bimetallic System at the Nanoscale: AgAu Sub-5 Nm Core–Shell Particles Studied at Atomic Resolution. *Nanoscale* **2018**, *10*, 2017–2024. https://doi.org/10.1039/c7nr07286d.
(37) Liao, T.-W.; Yadav, A.; Hu, K.-J.; van der Tol, J.; Cosentino, S.; D'Acapito, F.; Palmer, R. E.; Lenardi, C.; Ferrando, R.; Grandjean, D.; Lievens, P. Unravelling the Nucleation Mechanism of Bimetallic Nanoparticles with Composition-Tunable Core–Shell Arrangement. *Nanoscale* **2018**, *10*, 6684-6694-6684–6694. https://doi.org/10.1039/C8NR01481G.
(38) Neumeister, A.; Jakobi, J.; Rehbock, C.; Moysig, J.; Barcikowski, S. Monophasic Ligand-Free Alloy Nanoparticle Synthesis Determinants during Pulsed Laser Ablation of Bulk Alloy and Consolidated Microparticles in Water. *Phys Chem Chem Phys* **2014**, *16*, 23671–23678. https://doi.org/10.1039/C4CP03316G.
(39) Zhang, D.; Li, Z.; Sugioka, K. Laser Ablation in Liquids for Nanomaterial Synthesis: Diversities of Targets and Liquids. *J Phys Photonics* **2021**, *3*, 042002–042002. https://doi.org/10.1088/2515-7647/ac0bfd.
(40) Belić, D.; Chantry, R. L.; Li, Z. Y.; Brown, S. A. Ag-Au Nanoclusters: Structure and Phase Segregation. *Appl Phys Lett* **2011**, *99* (17), 171914–171914. https://doi.org/10.1063/1.3656244.
(41) Moreira, M.; Felix, L. C.; Cottancin, E.; Pellarin, M.; Ugarte, D.; Hillenkamp, M.; Galvao, D. S.; Rodrigues, V. Influence of Cluster Sources on the Growth Mechanisms and Chemical Composition of Bimetallic Nanoparticles. *J Phys Chem C* **2023**, *127*, 1944–1944. https://doi.org/10.1021/acs.jpcc.2c08044.
(42) Moreira, M.; Hillenkamp, M.; Rodrigues, V.; Ugarte, D. Ag Surface Segregation in Sub-10-Nm Bimetallic AuAg Nanoparticles Quantified by STEM-EDS and Machine Learning: Implications for Fine-Tuning Physicochemical Properties for Plasmonics and Catalysis Applications. *ACS Appl Nano Mater* **2024**, *7*, 1369–1378. https://doi.org/10.1021/acsanm.3c05495.
(43) Martínez, L. Adjustable Multimagnetron Approach. In *Gas-Phase Synthesis of Nanoparticles*; 2017; pp 101–121. https://doi.org/10.1002/9783527698417.ch6.
(44) Hoppe, S.; Müller, S. A First Principles Study on the Electronic Origins of Silver Segregation at the Ag-Au (111) Surface. *J Appl Phys* **2017**, *122*, 235303–235303. https://doi.org/10.1063/1.5017959.
(45) Chen, H.; Nabiei, F.; Badro, J.; Alexander, D. T. L.; Hébert, C. Non-Negative Matrix Factorization-Aided Phase Unmixing and Trace Element Quantification of STEM-

EDXS Data. *Ultramicroscopy* **2024**, *263*, 113981. https://doi.org/10.1016/j.ultramic.2024.113981.
(46) Chen, H.; Alexander, D. T. L.; Hébert, C. Leveraging Machine Learning for Advanced Nanoscale X-Ray Analysis: Unmixing Multicomponent Signals and Enhancing Chemical Quantification. *Nano Lett.* **2024**. https://doi.org/10.1021/acs.nanolett.4c02446.
(47) Brown, K. A.; Brittman, S.; Maccaferri, N.; Jariwala, D.; Celano, U. Machine Learning in Nanoscience: Big Data at Small Scales. *Nano Lett* **2020**, *20* (1), 2–10. https://doi.org/10.1021/acs.nanolett.9b04090.
(48) Spurgeon, S. R.; Ophus, C.; Jones, L.; Petford-Long, A.; Kalinin, S. V.; Olszta, M. J.; Dunin-Borkowski, R. E.; Salmon, N.; Hattar, K.; Yang, W.-C. D.; Sharma, R.; Du, Y.; Chiaramonti, A.; Zheng, H.; Buck, E. C.; Kovarik, L.; Penn, R. L.; Li, D.; Zhang, X.; Murayama, M.; Taheri, M. L. Towards Data-Driven next-Generation Transmission Electron Microscopy. *Nat Mater* **2021**, *20*, 274–274. https://doi.org/10.1038/s41563-020-00833-z.
(49) Tournus, F.; Tamion, A.; Blanc, N.; Hannour, A.; Bardotti, L.; Prével, B.; Ohresser, P.; Bonet, E.; Epicier, T.; Dupuis, V. Evidence of L10 Chemical Order in CoPt Nanoclusters: Direct Observation and Magnetic Signature. *Phys Rev B* **2008**, *77*, 144411–144411.
(50) Tamion, A.; Hillenkamp, M.; Hillion, A.; Tournus, F.; Tuaillon-Combes, J.; Boisron, O.; Zafeiratos, S.; Dupuis, V. Demixing in Cobalt Clusters Embedded in a Carbon Matrix Evidenced by Magnetic Measurements. *J Appl Phys* **2011**, *110*, 063904–063904. https://doi.org/10.1063/1.3638035.
(51) Okamoto, H.; Massalski, T. B. The Au-C (Gold-Carbon) System. *Bull Alloy Phase Diagr* **1984**, *5*, 378–378. https://doi.org/10.1007/BF02872953.
(52) Karakaya, I.; Thompson, W. T. The Ag-C (Silver-Carbon) System. *Bull Alloy Phase Diagr* **1988**, *9*, 226–226. https://doi.org/10.1007/BF02881268.
(53) Hillenkamp, M.; Di Domenicantonio, G.; Eugster, O.; Félix, C. Instability of Ag Nanoparticles in SiO2 at Ambient Conditions. *Nanotechnology* **2007**, *18*, 015702–015702. https://doi.org/10.1088/0957-4484/18/1/015702.
(54) Moreira, M.; Hillenkamp, M.; Divitini, G.; Tizei, L. H. G.; Ducati, C.; Cotta, M. A.; Rodrigues, V.; Ugarte, D. Improving Quantitative EDS Chemical Analysis of Alloy Nanoparticles by PCA Denoising: Part I, Reducing Reconstruction Bias. *Microsc Microanal* **2022**, *28*, 338–338. https://doi.org/10.1017/S1431927621013933.
(55) Moreira, M.; Hillenkamp, M.; Divitini, G.; Tizei, L. H. G.; Ducati, C.; Cotta, M. A.; Rodrigues, V.; Ugarte, D. Improving Quantitative EDS Chemical Analysis of AlloyNanoparticles by PCA Denoising: Part II. Uncertainty Intervals. *Microsc Microanal* **2022**, *28*, 723–723. https://doi.org/10.1017/S1431927622000551.
(56) Breyton, G.; Amara, H.; Nelayah, J.; Creuze, J.; Guesmi, H.; Alloyeau, D.; Wang, G.; Ricolleau, C. Atomic-Scale Surface Segregation in Copper-Gold Nanoparticles. *Phys Rev Lett* **2023**, *130*, 236201–236201. https://doi.org/10.1103/physrevlett.130.236201.
(57) Perich, M. P.; O'Connor, C. R.; Draijer, K. M.; Visser, N. L.; Artrith, N.; Reece, C.; Jongh, P. E. de; Hoeven, J. E. S. van der. In Situ Analysis of Gas Dependent Redistribution Kinetics in Bimetallic Au-Pd Nanoparticles. *J. Mater. Chem. A* **2024**. https://doi.org/10.1039/D4TA03030C.
(58) Tao, F.; Grass, M. E.; Zhang, Y.; Butcher, D. R.; Renzas, J. R.; Liu, Z.; Chung, J. Y.; Mun, B. S.; Salmeron, M.; Somorjai, G. A. Reaction-Driven Restructuring of Rh-Pd and Pt-Pd Core-Shell Nanoparticles. *Science* **2008**, *322* (5903), 932-934-932–934. https://doi.org/10.1126/science.1164170.
(59) Piccolo, L. Restructuring Effects of the Chemical Environment in Metal Nanocatalysis and Single-Atom Catalysis. *Catal Today* **2021**, *373*, 80–97. https://doi.org/10.1016/j.cattod.2020.03.052.

(60) Alayan, R.; Arnaud, L.; Bourgey, A.; Broyer, M.; Cottancin, E.; Huntzinger, J. R.; Lermé, J.; Vialle, J. L.; Pellarin, M.; Guiraud, G. Application of a Static Quadrupole Deviator to the Deposition of Size-Selected Cluster Ions from a Laser Vaporization Source. *Rev Sci Instrum* **2004**, *75*, 2461–2461. https://doi.org/10.1063/1.1764607.
(61) Olshin, P. K.; Sheardy, A. T.; Zhukovskyi, M. A.; Mukasyan, A. S. On the Atomic Scale Diffusion in Au–Ag Nanoparticles. *J Phys Chem C* **2024**, *128*, 4079–4085. https://doi.org/10.1021/acs.jpcc.3c08368.
(62) Jones, L.; Varambhia, A.; Beanland, R.; Kepaptsoglou, D.; Griffiths, I.; Ishizuka, A.; Azough, F.; Freer, R.; Ishizuka, K.; Cherns, D.; Ramasse, Q. M.; Lozano-Perez, S.; Nellist, P. D. Managing Dose-, Damage- and Data-Rates in Multi-Frame Spectrum-Imaging. *Microscopy* **2018**, *67*, i98–i113. https://doi.org/10.1093/jmicro/dfx125.
(63) Currie, L. A. Detection and Quantification Limits: Origins and Historical Overview1. *Anal. Chim. Acta* **1999**, *391* (2), 127–134. https://doi.org/10.1016/S0003-2670(99)00105-1.
(64) Cliff, G.; Lorimer, G. W. The Quantitative Analysis of Thin Specimens. *J Microsc* **1975**, *103* (2), 203–203. https://doi.org/10.1111/j.1365-2818.1975.tb03895.x.
(65) de la Peña, F.; Ostasevicius, T.; Fauske, V. T.; Burdet, P.; Jokubauskas, P.; Nord, M.; Sarahan, M.; Prestat, E.; Johnstone, D. N.; Taillon, J.; Caron, J.; Furnival, T.; MacArthur, K. E.; Eljarrat, A.; Mazzucco, S.; Migunov, V.; Aarholt, T.; Walls, M.; Winkler, F.; Donval, G.; Martineau, B.; Garmannslund, A.; Zagonel, L.-F.; Iyengar, I. Electron Microscopy (Big and Small) Data Analysis With the Open Source Software Package HyperSpy. *Microsc Microanal* **2017**, *23* (S1), 214–214. https://doi.org/10.1017/s1431927617001751.